Research Article Vol. 9, No. 4 / April 2022 / Optica 431

OPTICA

Planar wide-angle-imaging camera enabled by metalens array

Ji Chen,[1,2] Xin Ye,[1,2] Shenglun Gao,[1,2] Yuxin Chen,[1,2] Yunwei Zhao,[1,2] Chunyu Huang,[1] Kai Qiu,[1] Shining Zhu,[1,2] and Tao Li[1,2,*]

[1]National Laboratory of Solid State Microstructures, Key Laboratory of Intelligent Optical Sensing and Manipulations, Jiangsu Key Laboratory of Artificial Functional Materials, College of Engineering and Applied Sciences, Nanjing University, Nanjing, 210093, China
[2]Collaborative Innovation Center of Advanced Microstructures, Nanjing, 210093, China
*Corresponding author: taoli@nju.edu.cn

Received 15 October 2021; revised 23 January 2022; accepted 20 February 2022; published 14 April 2022

Wide-angle imaging is an important function in photography and projection, but it also places high demands on the design of the imaging components of a camera. To eliminate the coma caused by the focusing of large-angle incident light, traditional wide-angle camera lenses are composed of complex optical components. Here, we propose a planar camera for wide-angle imaging with a silicon nitride metalens array mounted on a CMOS image sensor. By carefully designing proper phase profiles for metalenses with intentionally introduced shifted phase terms, the whole lens array is capable of capturing a scene with a large viewing angle and negligible distortion or aberrations. After a stitching process, we obtained a large viewing angle image with a range of >120° using a compact planar camera. Our device demonstrates the advantages of metalenses in flexible phase design and compact integration, and the prospects for future imaging technology.

https://doi.org/10.1364/OPTICA.446063

1. INTRODUCTION

Complex optical components are utilized in various camera lenses to fulfill the growing requirements for imaging quality, which leads to bulky and heavy cameras. However, people also have high demands for the small size and portability of cameras. The recently developed metasurface is a kind of planar artificial material composed of sub-wavelength structural units [1–10]. Benefitting from flexible phase design advantages, the metasurface provides a promising way for miniaturization of imaging devices. Metalenses with only a single-layer of structure can realize functions comparable to traditional bulk refractive lenses. In recent years, metalenses with improved imaging performance such as achromatic metalenses have been designed to make them more applicable [11–19]. However, wide-angle imaging is difficult to realize with a single-layer metalens.

The wide-angle lens is in high demand owing to its capability of large information acquisition. Traditional wide-angle lenses (fisheye lenses) are composed of multiple refractive optical elements, which ensures the object light in a large viewing angle can be well imaged. Since the 1960s, with the wide application of optical automatic design technology, fisheye lenses have developed rapidly, and many lens structures with excellent imaging performance have appeared one after another. Many aberrations of the newly launched fisheye lens are well controlled, and the uniformity of its image surface illumination has also been significantly improved [20]. Although traditional optics has achieved great success, it still suffers problems such as heavy weight and large volume, obstructing the requirement for planarization and high integration of modern optical devices. To achieve a highly compact flat wide-angle view lens, many efforts have been tried to design a fisheye metalens. In principle, using a single-layer metalens with a certain phase profile to access a wide-angle imaging is impossible, since it requires the metalens to have different phase responses to different incident light [21]. Some designs based on planar lenses have been implemented to realize wide-angle imaging such as the metalens doublet [22,23], computational thin-plate lens [24,25], a metalens combined with an aperture [26,27], or compromises in focusing phase profiles [28,29]. However, these designs either have challenges in fabrication and computing resources, or sacrifice other imaging performances such as imaging efficiency or image resolution (see Supplement 1 Table S1 for detailed comparisons). In most previous works, metalenses act only as substitutes for traditional refractive lenses. In these works, the wide-angle imaging function still needs to be verified in a complex optical test system composed of an independent light source, detector, and other assistant optical components. Thus, a highly compact wide-angle imaging system based on a single-layer metalens with good performance has not been realized to date.

In this work, we propose a single-layer metalens array integrated wide-angle camera (MIWC) without sacrificing imaging performances. The phase of each metalens is carefully designed, by which incident light within a certain range of angles is imaged by each lens. These sub-images are then stitched into a complete wide-angle image. After characterizing the imaging properties of the metalens array with respect to the modulation transfer function (MTF), focusing efficiency, etc., we experimentally achieved

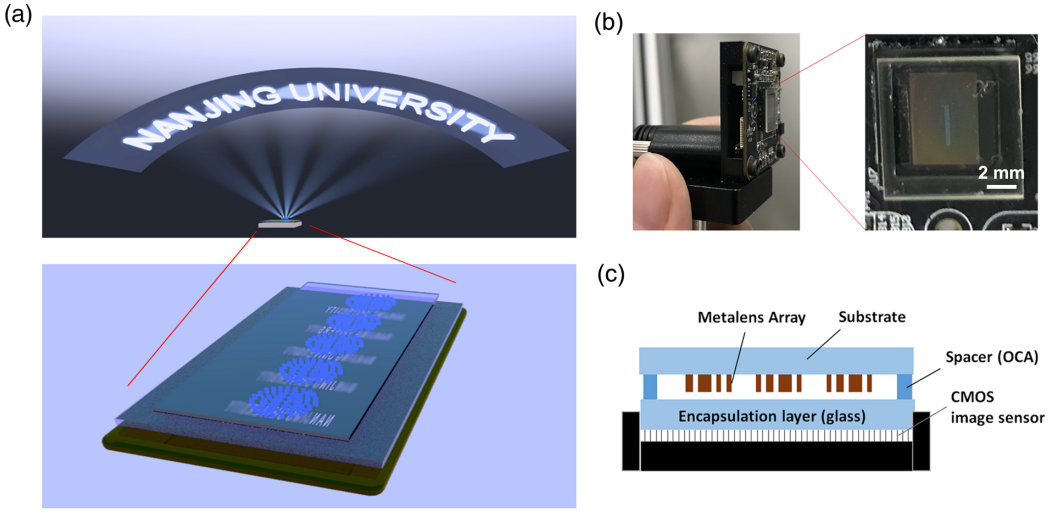

Fig. 1. Schematic diagram of the principle and device architecture. (a) Schematics of wide-angle imaging by MIWC. Zoom-in figure shows the imaging principle with each part of the wide-angle image clearly imaged separately by each metalens. (b) Photograph of MIWC. The metalens array can be seen in the middle of the enlarged figure on the right. (c) Architecture of MIWC. The metalens array is integrated directly on the CMOS image sensor (DMM 27UJ003-ML) and fixed by an optically clear adhesive (OCA) tape (Tesa, 69402).

wide-angle imaging of $>120°$. In addition, the metalens array is directly integrated onto the CMOS image sensor, which enables a compact, miniaturized, and stable camera that is quite promising in portable imaging devices, such as vehicle/airborne monitoring, remote sensing, detection, etc.

2. ARCHITECTURE OF MIWC

Figure 1(a) schematically shows an imaging scene. The metalens array was mounted directly on the CMOS image sensor, which is a one-dimensionally arranged metalens as shown in the zoom-in figure in Fig. 1(a). Each metalens is designed for a wavelength of 470 nm and is in charge of clearly imaging the object light within a certain viewing angle range. The clear imaging angle range of all metalenses can cover the entire $\pm 60°$ viewing angle, so the collected sub-images contain all the information that can be used to stitch together a complete wide-angle image. The MIWC device is shown in Fig. 1(b), and the size of the entire camera is about 1 cm × 1 cm × 0.3 cm. The structure of the metalens array can be clearly seen from the zoon-in image on the right. The device architecture is shown in Fig. 1(c). The metalens sample together with the substrate is directly mounted upside down on the CMOS image sensor (Imaging source, DMM 27UJ003-ML, pixel size: 1.67 μm) and fixed by an optically clear adhesive (OCA) tape (Tesa, 69402) [30]. The object light passes through the substrate and then modulated by the meatlens and imaged on the CMOS image sensor. The OCA tape with proper thickness is used to control the imaging distance with respect to focal designed metalenses. In our case, the camera works for far field imaging, and the imaging distance is approximately equal to the focal length of the metalens.

3. PHASE DESIGN OF METALENS ARRAY

In common cases, for perpendicular incident light, the phase profile of a focusing metalens is defined as

$$\phi(R) = \frac{2\pi}{\lambda}\left[f - \sqrt{f^2 + R^2}\right], \tag{1}$$

where R is the position in radius dimension from the lens center O, and f is the focal length. When the angle of incident light changes, this phase distribution is no longer suitable to focus the incident light perfectly, causing aberrations such as coma, astigmatism, and distortion. It is rightly the cause of all lenses having a limited field of view (FOV). For the focus case of oblique incident light, the phase profile should meet the condition [31]

$$\Delta\phi(R, \alpha) = -k\left[\Delta R \cdot \sin\alpha - \Delta R \cdot \sin\theta(R, \alpha)\right], \tag{2}$$

where $\Delta\phi$ is the phase difference of two infinitely close points at position R, ΔR is the distance of these two points, α is the angle of incident light, and θ is the angle of output light at position R, as shown in Fig. 2(a). The output angle θ is determined by the output position R, focus point position P, and focal length f with a relation of

$$\tan\theta(R, \alpha) = \left(\frac{P(\alpha) - R}{f}\right). \tag{3}$$

We define the focus point position $P(\alpha)$ as the projection function, because it determines the correspondence between the object point and image point. By inserting Eq. (3) into Eq. (2) and integrating on both sides of Eq. (2), we derive the target phase as

$$\phi(R, \alpha) = -k\left[R \cdot \sin\alpha + \sqrt{f^2 + (P(\alpha) - R)^2} - \sqrt{f^2 + P(\alpha)^2}\right]. \tag{4}$$

It can be seen from Eq. (4) that even at the same position R, the lens needs to have different phase responses to incident light of different angles, which is difficult to achieve in a single refractive lens or metalens. Here, the proposed lens array gives a good solution. In the lens design, there are several forms of projection functions, such as $P(\alpha) = 0$, $P(\alpha) = -f\tan\alpha$, $P(\alpha) = -f\alpha$, etc. The form of the projection function has a great influence on the imaging performance; see Supplement 1 Fig. S1 for details. Taking into account the imaging quality and imaging efficiency, we choose $P(\alpha) = -f\alpha$ as the projection function in the MIWC. The designed angles and FOV corresponding to each metalens are estimated and determined by aberrations analysis; see Supplement

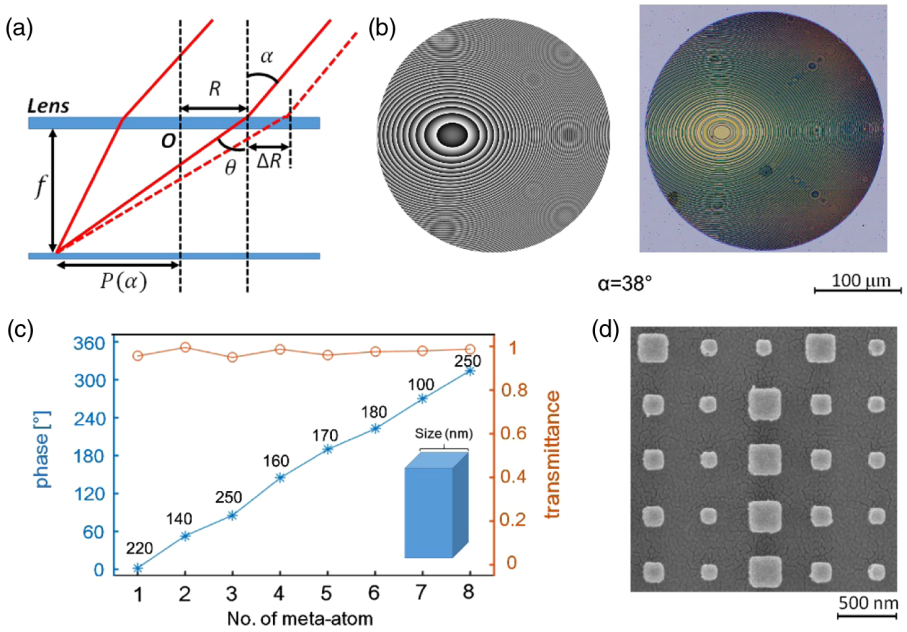

Fig. 2. Phase profiles and nano-structures of metalenses. (a) Schematic illustration of focusing oblique incident light by a metalens. The metalens is illuminated with parallel incident light at an angle of α with the optical axis. All incident light is focused at the focal plane and with a radial distance of $P(\alpha)$ from the lens center. (b) Phase distribution of metalens with designed angle of 38° (left) and corresponding optical microscope photograph (right). (c) Phase (blue stars) and transmittance (brown circles) of meta-atoms with eight different structural parameters, simulated by FDTD solutions. The sizes of the meta-atoms are marked along the phase distribution line, besides the blue stars. (d) Top-view SEM image of part of the fabricated metalens.

1 Fig. S2 for details. According to aberration analysis, the MIWC was determined to be composed of 17 lenses, the designed angles of which are 0°, ±19°, ±27°, ±33°, ±38°, ±43°, ±48°, ±53°, and ±57.5°. Considering the imaging intensity and imaging quality of the MIWC, we determined that the focal length and aperture diameter of each metalens are 450 μm and 300 μm, respectively. The lenses are arranged in one dimension and are close to each other. The final phase profile of each metalens can be calculated by substituting the corresponding designed angle and the lens parameters into Eq. (4).

The metalenses were fabricated in silicon nitride (Si_3N_4) nano-posts on a SiO_2 substrate. Different propagation phase modulations can be achieved by changing the structure parameters of meta-atoms, which is widely used in metasurface design [32–34]. Figure 2(b) shows the phase profiles and optical microscope photo of the lens with a designed angle of 38°. The meta-atom is a cuboid with a square cross section. Through finite difference time domain (FDTD) simulation, eight kinds of meta-atoms are selected to realize a phase shift over $0 - 2\pi$, and to ensure transmittance all over 90%. The sizes of the cross sections of these eight meta-atoms are shown in Fig. 2(c). The metalenses were fabricated using standard electron-beam lithography (EBL) and dry etching (see Section 5 for details). Figure 2(d) shows the top view of a scanning electron microscope (SEM) image of the metalens structure.

4. CHARACTERIZATION AND IMAGING PERFORMANCE OF MIWC

The performance of the MIWC was characterized at different incident angles with 470 nm laser illumination, where the focal spot, focusing efficiency, and MTFs are analyzed. For comparison, a traditional metalens with the same aperture diameter and focal length but a symmetric hyperbolic phase profile was also fabricated and measured. The experimental setup for characterizing focal spots corresponding to different incident angles is shown in Fig. 3(a), where a mirror is inserted to tune the incident angle. Figure 3(b) shows the focal spots of a traditional metalens and each metalens of MIWC for the corresponding incident angles. It is apparent that MIWC has a good focusing spot even if the incident angle increases to 57.5°. For traditional lenses, the focusing power diffuses quickly as the incident angle increases (even at 19°). Figure 3(c) plots the focusing efficiency of the angle-dependent metalenses of MIWC, which have a relatively high value of 65% for normal incidence, and still remain higher than 40% even in a large incident angle of 57.5°. To give a quantitative evaluation of imaging performance, the MTFs of the traditional lens and the MIWC are calculated from experimentally measured point spread functions (PSFs) as the results show in Fig. 3(d) and Fig. 3(e), respectively. It is well seen that the MTF from the traditional lens decays drastically at high frequencies from the incident angle of 19°, while those of MIWC lenses have relatively high values close to the diffraction limit even in the largest 57.5°. In fact, the comparison of MTFs corresponding to the traditional lens and MIWC can also be qualitatively obtained through theoretical analysis. For a lens, as long as it can focus incident light, it will implement the function of Fourier transform, through which the spatial information of the object is converted to spectral. The size of the lens focal spot mainly determines the cutoff frequency of the spectrum, which can be well represented by the MTF curve. For a traditional lens, the high-quality focusing of normal incident light leads to a 0° MTF curve close to the diffraction limited one, while the poor focusing of incident light at other angles leads to corresponding MTFs decaying rapidly as shown in Fig. 3(d). However, in MIWC, we solve this problem by using a metalens array, in which each lens has a designed angle and is responsible for a small range of imaging angles to guarantee good focusing performance within a small

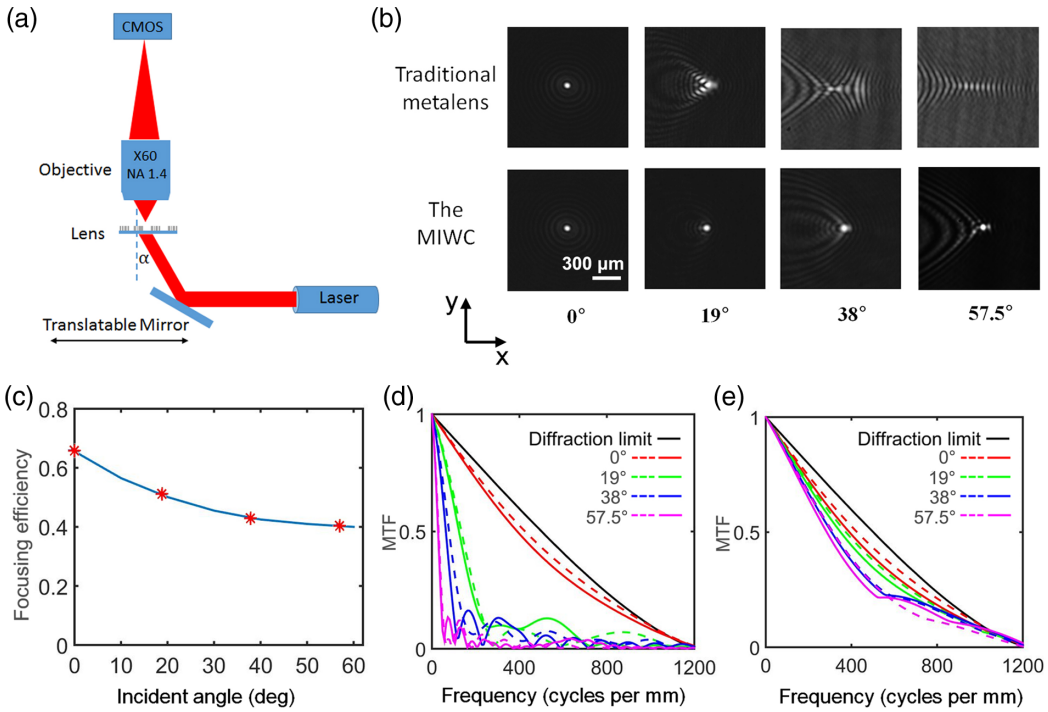

Fig. 3. Focusing performance of MIWC. (a) Schematic of the optical setup for testing focusing performance. Illuminating light on the lens is from a 470 nm laser and reflected by a mirror. Incident light at different angles can be achieved by translating and rotating the mirror. The focal spot of each metalens is amplified by an objective (×60, NA = 1.4) and imaged on a CMOS sensor. (b) Comparison of focal spots corresponding to a traditional metalens and MIWC with four different illuminating angles. (c) Focusing efficiency of MIWC for incident light with angles of 0°, 19°, 38°, and 57.5°. MTFs of (d) traditional metalens and (e) MIWC. The solid and dashed lines show MTFs in the tangential plane [along x axis in (b)] and sagittal plane [along y axis in (b)], respectively.

range. Thus, the MTFs corresponding to different incident angles are all close to the diffraction limited one, as shown in Fig. 3(e). So the experimental results of MTFs definitely demonstrate the overwhelming focusing advantage of MIWC over the traditional metalens in wide-angle incidences, which confirms the importance of our phase-shift metalens design for oblique incidences.

Before imaging specific wide-angle objects, we first verified the capability of the MIWC for angular position, that is, whether each lens can clearly image the target in the designed angular range. According to mirror symmetry, it is sufficient to check the performance by imaging targets only in positive angles. The objects to be imaged were projected on a curved screen. For high-efficiency imaging, the projected images were set to blue, which is closer to the designed wavelength of the metalens. A straight line projected on the curved screen was first selected as the object for characterization. This line is imaged by different lenses to form a group of sub-images, from which the lateral intensity profiles of the imaged lines at different positions should have correspondences to each lens. Specifically, we can determine the imaging angle and spanning range of a certain lens by judging the relatively small FWHM position of corresponding imaged lines. Figure 4(a) shows the sub-images corresponding to two lenses with designed angles of 0° and 48°. Two positions along the line were chosen for viewing the intensity distribution and the FWHM, as shown in Fig. 4(b). By analyzing the FWHM of the lateral intensity distribution at each position along the line and selecting the position with relatively small FWHM, the clear imaging area of the corresponding lens can be determined, as shown in Fig. 4(c). The complete sub-images and the analyzed clear imaging angular ranges are shown in Supplement 1 Fig. S3, from which it can be seen that the analyzed imaging angles are consistent with the designed ones.

To further confirm the imaging angle range of each lens, the letter "E" was projected onto the curved screen at different viewing angles for imaging [see Fig. 4(d)]. By checking the sub-images of the lens array, we can find the clearest and brightest sub-images located in the first row for normal incidence (0°) [left panel in Fig. 4(e)] and seventh row for 48° incidence [right panel in Fig. 4(e)]. More experimental results from all designed viewing angles are shown in Supplement 1 Fig. S4. It is found that the measured clearest imaging viewing angles are consistent with the designed angles of all lenses.

Afterwards, we carried out the experiment for a 120° imaging angle of view of the MIWC. Two projectors were used to display the words "NANJING UNIVERSITY" with a viewing angle covering 120° on the curved screen, which was imaged by the MIWC shown in Fig. 5(a). The images formed by lenses of −57°, 0°, and 57° are shown in Fig. 5(b) (see Supplement 1 Fig. S5 for complete experimental sub-images). It is easy to find that each lens can clearly image part of the wide-angle object, and the imaging range is determined by the designed angle of each lens. To stitch these blur-free image parts into a complete wide-angle image, a method based on a well-developed mask function processing is applied. The image formed by each lens has a corresponding mask function, shown as Fig. 5(c). The form of the mask functions are intensities with Gaussian distributions, the peak coordinates and standard deviation of which are determined by referring to the distributions shown in Fig. S3(b). Multiplying the sub-image and the corresponding mask function pixel by pixel can extract the clear imaging part of the sub-image, which is called the weighted

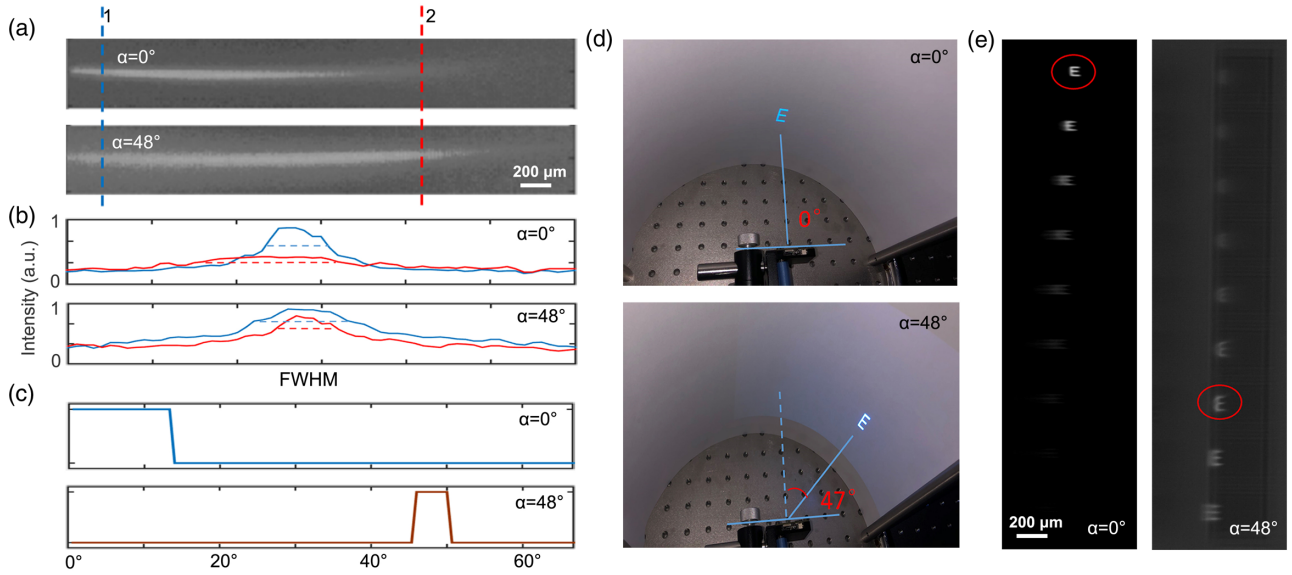

Fig. 4. Characterization of MIWC angular accuracy. (a) Imaging pattern of a straight line in two lenses with design angles of 0° and 48°. (b) Full width at half maxima (FWHM) of the lateral intensity at two positions marked with dashed lines in (a). The color of the intensity distribution curve corresponds to that of the dashed lines in (a). (c) Sharp imaging angular range of each lens by analyzing intensity FWHM distribution along the two imaged lines in (a). The analyzed angle range corresponds well with the designed ones. (d) Measurement of projected pattern's positions when it is imaged sharply by metalenses with designed angles of 0° and 48°. (e) Sharply imaged results of metalenses with designed angles of 0° and 48°.

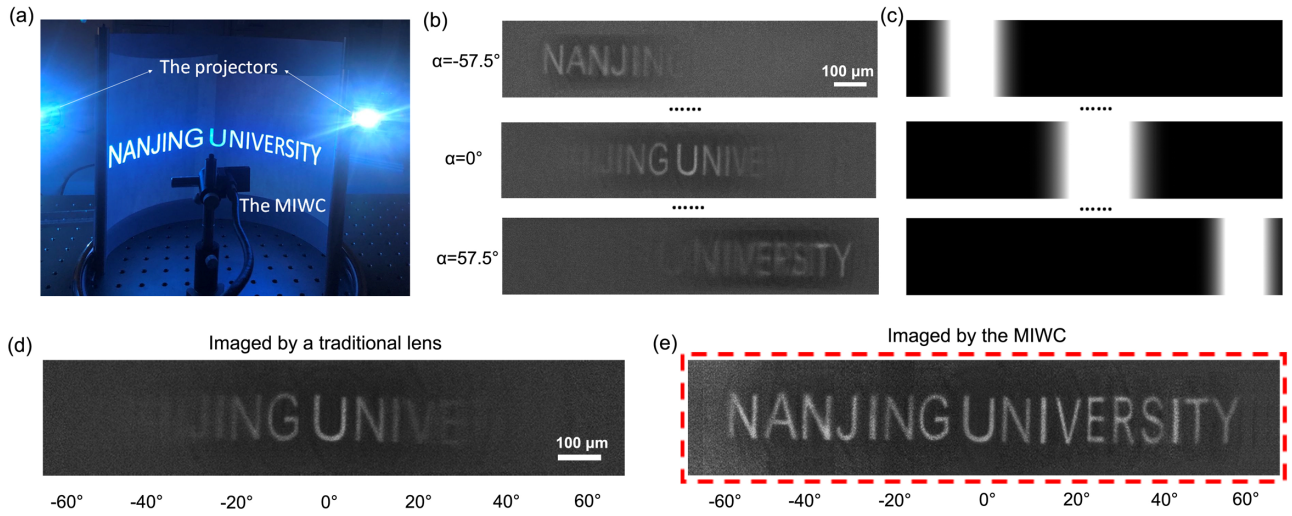

Fig. 5. Experimental wide-angle imaging results by MIWC. (a) Projected "NANJING UNIVERSITY" on the curved screen covers a viewing angle of 120° and then is imaged by MIWC. (b) Imaging results and corresponding mask functions of lenses with designed angles of −57.5°, 0°, 57.5°. (d) Imaging result of a traditional metalens showing limited field of view. (e) Final imaging result of MIWC by processing with mask functions and sub-images, which shows three times larger FOV compared with the traditional lens.

sub-image. By superimposing all weighted sub-images, we can get a stitched wide-angle image with background noise. To obtain the final high-quality wide-angle image, it is necessary to divide the result over the sum of the mask function. Supplement 1 Fig. S6 shows the stitching process in detail. Finally, the ultimate wide-angle image is achieved, shown in Fig. 5(e), which clearly exhibits every letter of "NANJING UNIVERSITY." To further show the wide-angle performance, we compare it with the image of a traditional metalens [see Fig. 5(d)] with a traditional hyperbolic phase profile. It is evident that the traditional lens can image clearly only with an angle range within ±20°, which is one third of the capability of the MIWC.

5. MATERIALS AND METHODS

A. Device Fabrication

By using plasma enhanced chemical vapor deposition (PECVD), the silicon nitride layer with a final thickness of 1000 nm was deposited on the fused-silica substrate, and 200 nm PMMA A4 resist film was then spin coated onto the substrate and baked at 170°C for 5 min. A 42 nm thick layer of water-soluble conductive polymer (AR-PC 5090) was spin coated on the resist for the dissipation of E-beam charges. The device pattern was next written by using an E-beam writer (Elionix ELS-F125). The conductive polymer was then dissolved in water, and resist was developed in a resist developer solution. An electron beam evaporated chromium

layer was used to reverse the generated pattern with a liftoff process, and was then used as a hard mask for dry etching the silicon nitride layer. The dry etching was performed in a mixture of CHF3 and SF6 plasmas using an inductively coupled plasma reactive ion etching process (Oxford Instruments, PlasmaPro100 Cobra300). Finally, the chromium layer was removed by a stripping solution (ceric ammonium nitrate).

B. Ray Tracing Simulation

Ray tracing simulation can be used not only to theoretically determine the direction of emitted light corresponding to incident light at different angles, but also further used to simulate the focal spots of the metalenses. The simulation is based on the generalized Snell's law, according to which light rays propagating to an interface will obey the relationship as follows:

$$\sin(\theta_t) - \sin(\theta_i) = \frac{\lambda}{2\pi}\frac{\mathrm{d}\phi}{\mathrm{d}r}, \tag{5}$$

where θ_t and θ_i are the angle of refraction and incidence, respectively, and r is the incident position of light on the metalens. According to Eq. (5), the propagation of light passing through a metalens can be completely determined. This ray tracing simulation was applied to calculate the light traveling path in Supplement 1 Fig. S1. By collecting the refractive light distribution on the focal plane, the shape of the focal spots can be obtained, as shown in Supplement 1 Fig. S2.

6. DISCUSSION AND CONCLUSION

In the MIWC, the imaging element is designed as a one-dimensional metalens array considering the following reasons. Although a two-dimensional lens array can expand the viewing angle in both horizontal and vertical dimensions, the number of CMOS pixels and the imaging cross talk between lenses will limit the range of the viewing angle in the two dimensions. The one-dimensional lens can ensure that the viewing angle will not be restricted in the horizontal direction. On the other hand, the experimental results show that without any special phase design, a lens already has a viewing angle of near $\pm 20°$, which is sufficient for the longitude viewing angle in many applications, for example, the wide-angle photography of landscapes and wide-angle detection in autonomous driving. Thus, this kind of one-dimensional wide-angle imaging already has enough application value. However, two-dimensional wide-angle imaging cannot be simply extended from the one-dimensional design, because the metalens we propose has no rotation symmetry like traditional lenses. If the viewing angle is to be extended in the longitudinal direction, one can design two or three groups of the horizontal one-dimensional lens array, by adding an additional phase corresponding to the longitudinal viewing angle in each group. Therefore, it is possible to increase the longitudinal viewing angle to some extent.

In theory, as long as the number of metalenses is sufficient, our design can achieve a viewing angle of $\pm 90°$. However, in an actual imaging scene, the irradiation cross section of the large-angle light on a planar lens is very small, resulting in low luminance of the large-angle object light. Thus, in our experiment, to get good imaging quality, we show a wide viewing angle of only $\pm 60°$. In the traditional fisheye lens, this problem is solved by designing a large-curved lens to receive more light from a large viewing angle. However, when fabrication technology further develops, in our design, the fabricated metalens array can also be arranged on a curve shaped substrate to solve this problem. But this solution is difficult to realize in works using single large-sized metalenses, since fabricating the entire metalens on a curved substrate places extremely high requirements on fabrication capabilities.

In conclusion, we have proposed and implemented a highly compact wide-angle imaging device by mounting a well-designed planar metalens array onto a CMOS sensor. Each metalens within the array accounts for a certain range of wide-angle incidence, which in principle circumvents the difficulty of a single-phase profile for whole wide-angle view in common designs. Imaging performances of the integrated device, including focusing efficiency, MTF, resolution, and angular accuracy, were systematically investigated. Finally, we used 17 lenses to compose an array camera and obtained a 120°-wide viewing angle, which is the largest one with a clear real image by a flat lens, to our knowledge. This good performance significantly attributes to the flexible engineering of metalenses, where a phase-shift design is introduced that grants each lens good image quality. The remarkably improved MTF compared with a traditional metalens well confirms the advantage of our design. Moreover, our approach provides a very compact flat camera with the lens array distributed scheme, which works not only for a wide-angle flat camera with broad application potentials, but also would inspire new explorations in space-multiplexed spectral imaging, sensing, and other functionalities.

Funding. National Key Research and Development Program of China (2016YFA0202103); National Natural Science Foundation of China (91850204, 12104223); Dengfeng Project B of Nanjing University.

Disclosures. The authors declare no conflicts of interest.

Author Contributions. T. L. and J. C. developed the idea. J. C. proposed the design and performed the numerical simulation. S. G. and Y. C. fabricated the samples with help from C. H. and K. Q. J. C. performed the optical measurement with assistance from X. Y. T. L. supervised the project. J. C., Y. Z., and T. L. analyzed the results. J. C. and T. L. wrote the manuscript. All authors contributed to discussions.

Data availability. Data underlying the results presented in this paper are not publicly available at this time but may be obtained from the authors upon reasonable request.

Supplemental document. See Supplement 1 for supporting content.

REFERENCES

1. D. Lin, P. Fan, E. Hasman, and M. L. Brongersma, "Dielectric gradient metasurface optical elements," Science **345**, 298–302 (2014).
2. N. Yu and F. Capasso, "Flat optics with designer metasurfaces," Nat. Mater. **13**, 139–150 (2014).
3. N. Meinzer, W. L. Barnes, and I. R. Hooper, "Plasmonic meta-atoms and metasurfaces," Nat. Photonics **8**, 889–898 (2014).
4. A. Arbabi, Y. Horie, M. Bagheri, and A. Faraon, "Dielectric metasurfaces for complete control of phase and polarization with subwavelength spatial resolution and high transmission," Nat. Nanotechnol. **10**, 937–943 (2015).
5. X. Ni, Z. J. Wong, M. Mrejen, Y. Wang, and X. Zhang, "An ultrathin invisibility skin cloak for visible light," Science **349**, 1310–1314 (2015).
6. G. Zheng, H. Mühlenbernd, M. Kenney, G. Li, T. Zentgraf, and S. Zhang, "Metasurface holograms reaching 80% efficiency," Nat. Nanotechnol. **10**, 308–312 (2015).
7. J. Chen, T. Li, S. Wang, and S. Zhu, "Multiplexed holograms by surface plasmon propagation and polarized scattering," Nano Lett. **17**, 5051–5055 (2017).
8. J. P. B. Mueller, N. A. Rubin, R. C. Devlin, B. Groever, and F. Capasso, "Metasurface polarization optics: independent phase control of arbitrary orthogonal states of polarization," Phys. Rev. Lett. **118**, 113901 (2017).

9. J. Chen, X. Chen, T. Li, and S. Zhu, "On-chip detection of orbital angular momentum beam by plasmonic nanogratings," Laser Photon. Rev. **12**, 1700331 (2018).
10. A. Overvig and A. Alù, "Wavefront-selective Fano resonant metasurfaces," Adv. Photon. **3**, 026002 (2021).
11. F. Aieta, M. A. Kats, P. Genevet, and F. Capasso, "Multiwavelength achromatic metasurfaces by dispersive phase compensation," Science **347**, 1342–1345 (2015).
12. M. Khorasaninejad, W. T. Chen, R. C. Devlin, J. Oh, A. Y. Zhu, and F. Capasso, "Metalenses at visible wavelengths: diffraction-limited focusing and subwavelength resolution imaging," Science **352**, 1190–1194 (2016).
13. S. Wang, P. C. Wu, V.-C. Su, Y.-C. Lai, C.-H. Chu, J.-W. Chen, S.-H. Lu, J. Chen, B. Xu, C.-H. Kuan, T. Li, S. Zhu, and D. P. Tsai, "Broadband achromatic optical metasurface devices," Nat. Commun. **8**, 187 (2017).
14. S. Wang, P. C. Wu, V.-C. Su, Y.-C. Lai, M.-K. Chen, H. Y. Kuo, B. H. Chen, Y. H. Chen, T.-T. Huang, J.-H. Wang, R.-M. Lin, C.-H. Kuan, T. Li, Z. Wang, S. Zhu, and D. P. Tsai, "A broadband achromatic metalens in the visible," Nat. Nanotechnol. **13**, 227–232 (2018).
15. W. T. Chen, A. Y. Zhu, V. Sanjeev, M. Khorasaninejad, Z. Shi, E. Lee, and F. Capasso, "A broadband achromatic metalens for focusing and imaging in the visible," Nat. Nanotechnol. **13**, 220–226 (2018).
16. R. J. Lin, V.-C. Su, S. Wang, M. K. Chen, T. L. Chung, Y. H. Chen, H. Y. Kuo, J.-W. Chen, J. Chen, Y.-T. Huang, J.-H. Wang, C. H. Chu, P. C. Wu, T. Li, Z. Wang, S. Zhu, and D. P. Tsai, "Achromatic metalens array for full-colour light-field imaging," Nat. Nanotechnol. **14**, 227–231 (2019).
17. C. Chen, W. Song, J.-W. Chen, J.-H. Wang, Y. H. Chen, B. Xu, M.-K. Chen, H. Li, B. Fang, J. Chen, H. Y. Kuo, S. Wang, D. P. Tsai, S. Zhu, and T. Li, "Spectral tomographic imaging with aplanatic metalens," Light Sci. Appl. **8**, 99 (2019).
18. H. Kwon, E. Arbabi, S. M. Kamali, M. Faraji-Dana, and A. Faraon, "Single-shot quantitative phase gradient microscopy using a system of multifunctional metasurfaces," Nat. Photonics **14**, 109–114 (2020).
19. Z. Shen, S. Zhou, X. Li, S. Ge, P. Chen, W. Hu, and Y. Lu, "Liquid crystal integrated metalens with tunable chromatic aberration," Adv. Photon. **2**, 036002 (2020).
20. H. Sato, "Fisheye lens having a short distance compensating function," U. S. patent 5434713 (18 July 1995).
21. X. Luo, F. Zhang, M. Pu, Y. Guo, X. Li, and X. Ma, "Recent advances of wide-angle metalenses: principle, design, and applications," Nanophotonics **11**, 1–20 (2022).
22. A. Arbabi, E. Arbabi, S. M. Kamali, Y. Horie, S. Han, and A. Faraon, "Miniature optical planar camera based on a wide-angle metasurface doublet corrected for monochromatic aberrations," Nat. Commun. **7**, 13682 (2016).
23. B. Groever, W. T. Chen, and F. Capasso, "Meta-lens doublet in the visible region," Nano Lett. **17**, 4902–4907 (2017).
24. Y. Peng, Q. Sun, X. Dun, G. Wetzstein, W. Heidrich, and F. Heide, "Learned large field-of-view imaging with thin-plate optics," ACM Trans. Graph. **38**, 219 (2019).
25. C. Hao, S. Gao, Q. Ruan, Y. Feng, Y. Li, J. K. W. Yang, Z. Li, and C.-W. Qiu, "Single-layer aberration-compensated flat lens for robust wide-angle imaging," Laser Photon. Rev. **14**, 2000017 (2020).
26. J. Engelberg, C. Zhou, N. Mazurski, J. Bar-David, A. Kristensen, and U. Levy, "Near-IR wide-field-of-view Huygens metalens for outdoor imaging applications," Nanophotonics **9**, 361–370 (2020).
27. M. Y. Shalaginov, S. An, F. Yang, P. Su, D. Lyzwa, A. M. Agarwal, H. Zhang, J. Hu, and T. Gu, "Single-element diffraction-limited fisheye metalens," Nano Lett. **20**, 7429–7437 (2020).
28. M. Pu, X. Li, Y. Guo, X. Ma, and X. Luo, "Nanoapertures with ordered rotations: symmetry transformation and wide-angle flat lensing," Opt. Express **25**, 31471–31477 (2017).
29. A. Martins, K. Li, J. Li, H. Liang, D. Conteduca, B.-H. V. Borges, T. F. Krauss, and E. R. Martins, "On metalenses with arbitrarily wide field of view," ACS Photon. **7**, 2073–2079 (2020).
30. B. Xu, H. Li, S. Gao, X. Hua, C. Yang, C. Chen, F. Yan, S. Zhu, and T. Li, "Metalens-integrated compact imaging devices for wide-field microscopy," Adv. Photon. **2**, 066004 (2020).
31. A. Kalvach and Z. Szabó, "Aberration-free flat lens design for a wide range of incident angles," J. Opt. Soc. Am. B **33**, A66–A71 (2016).
32. R. C. Devlin, A. Ambrosio, N. A. Rubin, J. P. B. Mueller, and F. Capasso, "Arbitrary spin-to-orbital angular momentum conversion of light," Science **358**, 896–901 (2017).
33. N. A. Rubin, A. Zaidi, M. Juhl, R. P. Li, J. P. B. Mueller, R. C. Devlin, K. Leosson, and F. Capasso, "Polarization state generation and measurement with a single metasurface," Opt. Express **26**, 21455–21478 (2018).
34. F. Dong, H. Feng, L. Xu, B. Wang, Z. Song, X. Zhang, L. Yan, X. Li, W. Wang, L. Sun, Y. Li, and W. Chu, "Information encoding with optical dielectric metasurface via independent multichannels," ACS Photon. **6**, 230–237 (2019).